

Enhanced Backgate Tunability on Interfacial Carrier Concentration in Ionic Liquid-Gated MoS₂ Devices

Qiao Chen¹, Chengyu Yan^{*,1,2}, Changshuai Lan¹, Qiyang Song¹, Yi Yan¹, Shun Wang^{*,1,2}

¹MOE Key Laboratory of Fundamental Physical Quantities Measurement & Hubei Key Laboratory of Gravitation and Quantum Physics, National Gravimetry Laboratory and School of Physics, Huazhong University of Science and Technology, Wuhan 430074, China

²Institute for Quantum Science and Engineering, Huazhong University of Science and Technology, Wuhan 430074, China

Corresponding Authors: Chengyu Yan (chengyu_yan@hust.edu.cn); Shun Wang (shun@hust.edu.cn)

Abstract

The periodic spatial modulation potential arising from the zig-zag distribution of ions at large gate voltage in an ionic liquid gated device may enable functionalities in a similar way as nanopatterning and moiré engineering. However, the inherent coupling between periodic modulation potential and carrier concentration in ionic liquid devices has hindered further exploration. Here, we demonstrate the feasibility of decoupling manipulation on periodic modulation potential and carrier density in an ionic liquid device by using a conventional backgate. The backgate is found to have a tunability on carrier concentration comparable to that of ionic gating, especially at large ionic liquid gate voltage, by activating the bulk channels mediated back tunneling between the trapped bands and interfacial channel.

1. Introduction

Imprinting a periodic spatial modulation potential, with a periodicity different from the lattice periodicity of the hosting material, to a two-dimensional electronic system has stimulated development in emerging optical and electronic functionalities^[1-5] owing to the enhanced light-matter interactions^[1, 6-8] and electron-electron correlations^[5, 9, 10]. Nanopatterning and moiré engineering are the most common approaches to induce the periodic modulation^[2, 11, 12]. Enormous efforts are being dedicated to these two approaches to enrich the tunability^[13-17], including tuning the strength and periodicity of the modulation potential *in situ*. Interestingly, the *in situ* control over the strength and periodicity of the modulation potential can potentially be implemented via an alternative approach, i.e., ionic liquid gating at large gate voltage. Ionic liquid gating is most well-known for its capability of inducing massive amount of charge carriers at the interface^[18-30], whereas its implication in generating periodic spatial modulation potential is somehow overlooked. Here, applying a large gate voltage will enforce the spatial distribution of ions undertake a transition from a uniform one to a zig-zag one, as illustrated in Figure 1a, to minimize the repulsion between the densely packed ions, which can be verified through topographic characterization^[31-36], and theoretical simulation^[37-42]. The zig-zag distributed ions in turn cast a spatially modulated potential to the two-dimensional system. The strength and periodicity of the modulation potential can be manipulated via the distribution of ions or equivalently speaking the gate voltage. Experimentally, the spatial modulation manifests itself via the formation of trapped bands or states at certain ionic liquid gate voltage^[31, 43-46]. However, it is necessary to stress that the manipulation on the spatial modulation potential via ionic liquid gating does not warrant that one can realize similar functionalities enabled by nanopatterning or moiré engineering. In the case of nanopatterning or moiré engineering, the control over periodic modulation potential and carrier concentration, which are perhaps equally important in a wide range of applications, can be adjusted independently^[13, 14]. In contrast, the manipulation on these two quantities is coupled together in the case of ionic liquid gating. It is therefore highly

desirable to supplement the ionic liquid gating with additional control knobs.

Backgate seems to be a natural candidate at first glance since it provides extra control on the carrier concentration. However, from the perspective of capacitive effect, a conventional backgate has little impact in an ionic gated device, considering the electric field due to the backgate is negligible in comparison with the colossal one due to the ionic liquid gate^[18, 30, 43, 47, 48]. Although there are also attempts of achieving sizable modulation on carrier concentration by unconventional backgates such as ionic solid gate^[49, 50], the long-term stability and complementary metal oxide semiconductor (CMOS) compatibility of these unconventional backgates are still to be optimized. Fortunately, a conventional backgate can possibly participate the modulation of charge carriers in an indirect manner other than direct charging effect. For instance, it is demonstrated in a dual-gated polymer conductor that the weak electric field due to the backgate can perturb the Coulomb gap induced by ionic liquid, which results in a much larger change in the tunability compared to the expectation of the capacitive effect^[44].

In this work, we demonstrate that a conventional backgate can lead to a modulation in the carrier concentration comparable to ionic liquid gate itself in a dual gated transition metal dichalcogenides (TMDs) device via indirect approach. It is indeed unlikely for the backgate to directly affect the interfacial channel, however, it can populate or deplete the bulk channels that mediate the back tunneling process between the interfacial channel and trapped bands, and hence notably tuning the transport property at the interface. As a result, our work highlights the possibility of decoupled control on periodic potential and carrier concentration in an ionic liquid gated device, and thus may accelerate advanced architecture that harnesses the extremely high carrier concentration and tunable periodic modulation potential at the same time.

2. Result and discussion

2.1 Emergence of Trapped Bands

MoS₂ flakes, etched into standard Hall bars, are dual-gated by an ionic liquid DEME-TFSI (N,N-diethyl-N-methyl-N-(2-methoxyethyl) ammonium bis

(trifluoromethylsulfonyl)-imide) on the top and a heavily doped Si backgate at the bottom. We first characterize the impact of ionic gate, with backgate grounded, in flakes with various thickness. Figure 1b depicts the transfer curve against the ionic gate voltage (V_{ig}) of a typical device with a thickness of 10 nm. It is seen that the drain current (I_d) initially rises with increasing V_{ig} up to $V_{ig} = 3$ V, then gradually decays and saturates, in line with previous reports^[18, 51, 52]. The reduction and saturation of I_d with large V_{ig} are usually attributed to electrochemical reaction between the ionic liquid and devices under test^[21, 44, 46]. However, it is ought to highlight that the electrochemical reaction is irreversible and thus the transfer curves should be diverse after repeating the measurements. Transfer curves in our experiments, on the other hand, almost overlay through different runs (see *Support Information* section 2 for details). Instead, the behavior in large V_{ig} regime signifies the emergence of trapped bands, due to the spatial redistribution of ions driven by the ionic gate voltage, at the interface between the ionic liquid and MoS₂, analogous to the trapped bands observed in WS₂ devices^[43]. This interpretation based on trapped bands can be verified experimentally.

First, localization of charge carrier becomes increasingly profound at larger V_{ig} . This effect will compete with the charge accumulation due to the conventional capacitive effect, and may therefore result in a non-monotonic evolution of the concentration n_{2D} of mobile charge carrier with respect to V_{ig} . We indeed observed a non-monotonic n_{2D} - V_{ig} relation, in good correlation with the evolution of I_d , as highlighted in Figure 1b. In addition, it is noteworthy that all transfer curve measurements in this study were systematically conducted at 220 K, whereas the n_{2D} derived from Hall effect were obtained at 165 K (see *Experimental Section* for details). Second, the trapped bands can interplay with the interfacial states via an indirect back tunneling process mediated by the bulk channels. Here, the localized charge carriers of the trapped bands first hop into the partially populated bulk channels in the case of MoS₂, other materials may behave differently as we will demonstrate later on, and then return to the interfacial channels to contribute to I_d , as shown in Figure 1c. In this regard, the back tunneling effectively weakens the influence of localization. The probability of back tunneling process can be tuned by the number of bulk channels

which is directly related to the thickness of the flakes in the case of MoS₂. It is then expected that I_d at large V_{ig} should be increased with enhanced back tunneling in a thicker flake with more bulk channels, since less charge carriers are effectively localized. This prediction is in good agreement with the experimental observation that I_d/I_{peak} , I_{peak} is the maximum value of I_d for a given flake thickness, saturates at larger value with increasing flake thickness, as shown by the raw data in Figure 1d or linear-rescaled data in Figure 1e after taken the variation in ionic liquid gate capacitance into account (see *Support Information* section 5 for details).

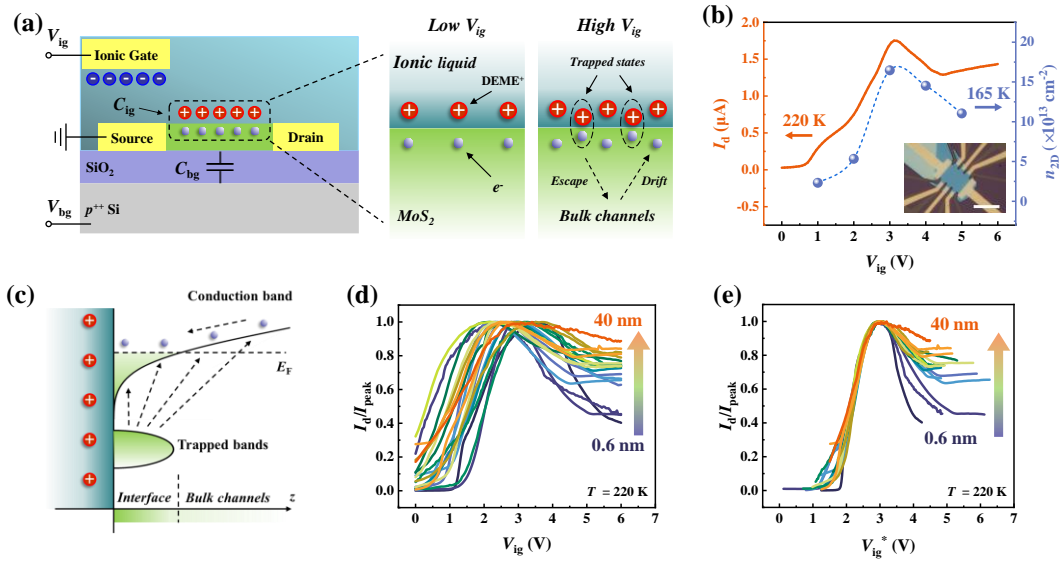


Figure 1. Trapped bands in an ionic-MoS₂ device and back tunneling process. a) Schematic representation of the ionic-MoS₂ device and ion distribution at the interface. The green channel denotes MoS₂ crystal, the blue spheres indicate anions TFSI⁻, the red spheres represent cations DEME⁺, and the grey spheres indicate electrons. Charge carriers are localized due to the zig-zag distribution of ions at large V_{ig} as shown in the ellipses. b) Transfer characteristics curve ($V_d = 10$ mV) and carrier density of the 10 nm ionic-MoS₂ device. Inset: the optical image of the device, the scale bar is 10 μ m. c) Energy band of the ionic-MoS₂ device, with the x-axis representing the z-direction of the MoS₂ crystal. d) Transfer characteristic curves of ionic-MoS₂ devices with various thicknesses. e) Transfer characteristic curves after scaling $V_{ig}^* = \alpha \times V_{ig} - V_{offset}$ to eliminate the impact due to variation in the ionic liquid gate capacitance and intrinsic doping, here both α and V_{offset} are sample specific.

2.2 Tuning Back Tunneling Process with a Backgate

Interestingly, the back tunneling process opens a new venture to modulate the transport property of the interfacial channels with a backgate. The backgate can

contribute via tuning the bulk channels. Apply a positive backgate voltage (V_{bg}) tends to populate the bulk channels and hence blocks the back tunneling, so that more charge carriers would be localized at the trapped bands and thus results in a reduction of n_{2D} of mobile carriers. On the other hand, a negative V_{bg} enhances the back tunneling process via depleting the bulk channels, which in turn leads to an increase in n_{2D} .

Our experimental results follow the prediction. The measurements with both ionic liquid gate and backgate activated were carried out at 165 K, far below the glass transition of ionic liquid DEME-TFSI. It is necessary to stress that backgate voltage is applied after the ionic liquid has already been frozen, hence the backgate voltage does not perturb the distribution of ions^[53]. Let us first focus on the result in a flake with a thickness of 10 nm. At low V_{ig} , where the trapped bands are not well established, sweeping backgate voltage does not cause noticeable change in n_{2D} evidenced as Δn_{2D} is almost pinned to zero, $\Delta n_{2D}(V_{bg}, V_{ig}) = n_{2D}(V_{bg}, V_{ig}) - n_{2D}(0, V_{ig})$, regardless of the polarity of V_{bg} in Figure 2a. A weak linear dependence of Δn_{2D} on V_{bg} is discernible upon closer examination, originating from the conventional capacitive coupling of the backgate. Gradually increase V_{ig} will drive the formation of trapped bands. With the formation of trapped bands, it is found that V_{bg} can change Δn_{2D} dramatically. Additional carrier concentration on the order of $10 \times 10^{13} \text{ cm}^{-2}$ can be supplemented to the system at $V_{ig} > 3 \text{ V}$ (when trapped bands are firmly established) with negative V_{bg} , comparable to the carrier concentration induced by the ionic liquid gate itself at the corresponding voltage. Positive V_{bg} leads to a reduction of carrier concentration on the order of $1 \times 10^{13} \text{ cm}^{-2}$ at large V_{ig} . The observation that negative V_{bg} adds charge carriers whereas positive one removes carriers agrees with the back tunneling model, but in staggering contrast to the standard functionality of a backgate based on the capacitive model. The aforementioned trend may be more easily recognized after presenting the data in a complementary manner, i.e., n_{2D} as a function of V_{ig} at fixed V_{bg} , as depicted in Figure 2b. It is clear that traces with positive V_{bg} mimic the intrinsic behavior of an ionic liquid tuned device ($V_{bg} = 0 \text{ V}$) until $V_{ig} \sim 3 \text{ V}$, then reduction in n_{2D} due to trapped bands becomes more effective with positive V_{bg} . On the contrary, negative V_{bg} not only induces sizable additional charge carrier, pushing n_{2D} to an enormous value of 35×10^{13}

cm^{-2} , but also delays the full dominance of the trapped bands to $V_{\text{ig}} = 4 \text{ V}$.

Qualitatively similar results have been systemically verified in flakes with thickness spanning from 1.8 nm to 80 nm as summarized in Figure 2c & d. The effectiveness of the backgate is rather sensitive to the thickness of the flakes. The backgate is most efficient in flakes with an intermediate thickness around 10 nm, whereas its impact decays when the thickness approaches both few-layer limit and bulk limit. In the few-layer limit, there is rather limited number of bulk channels to start with, the back tunneling of the localized charge carriers is quite restricted regardless of the occupation of the bulk channels, hence the backgate is not influential. In the bulk limit, the backgate primarily modules the bulk channels near the bottom surface, its tunability on the bulk channels in the close vicinity of the ionic liquid-MoS₂ interface, that really matters to the back tunneling process, is largely screened, hence the backgate is again non-efficient. Nevertheless, the backgate tunability still exceeds that expected from the capacitive effect even in the few-layer limit or bulk limit, companied with reversed polarity.

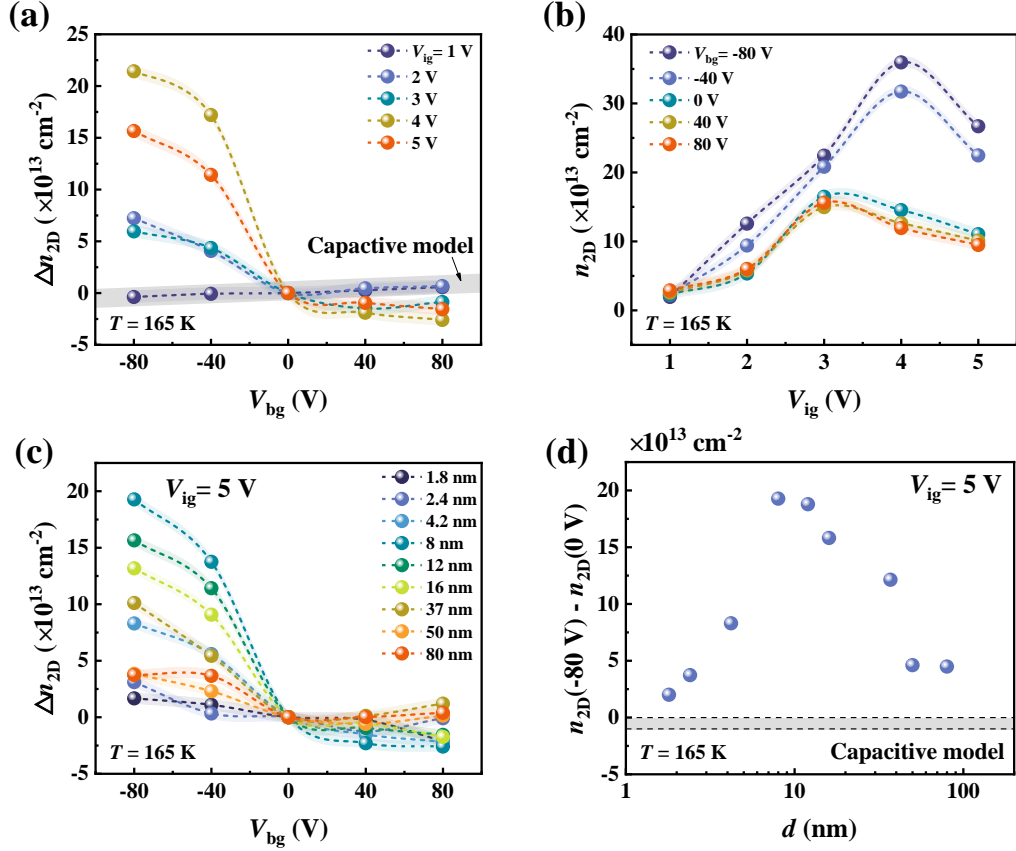


Figure 2. Demonstration of efficient tunability on carrier concentration via a backgate at 165 K. a) The response of relative carrier concentration Δn_{2D} to V_{bg} with incremented V_{lg} , $\Delta n_{2D}(V_{bg}, V_{lg}) = n_{2D}(V_{bg}, V_{lg}) - n_{2D}(0, V_{lg})$, in a 10 nm flake, grey strip indicates the tunability based on the conventional capacitive model of backgate. b) The response of n_{2D} to V_{lg} with fixed V_{bg} . c) Δn_{2D} as a function of V_{bg} at $V_{lg} = 5$ V in flakes with different thickness. d) Backgate tunability as a function of flakes thickness at $V_{bg} = -80$ V, grey strip indicates the tunability based on the conventional capacitive model of backgate.

2.3 Necessary Electronic Properties of Achieving Notable Backgate Tunability

Since the presence of the bulk channels and their occupancy are crucial to the back tunneling process, it is interesting to analyse the behavior in different TMDs especially in large V_{lg} regime. Here, we take WS_2 and WSe_2 as examples. Trapped bands also forms in these two materials at large V_{lg} in a similar manner as that observed in MoS_2 (see *Support Information* section 7 for details). However, thickness dependence data and backgate tunability data shows qualitatively different behavior in WS_2 and WSe_2 with respect to MoS_2 .

Figure 3 summarizes the thickness dependence data. Figures 3a & b show the

transfer characteristics of WS₂ and WSe₂ devices using the same linear-rescaling as for MoS₂ (see *Support Information* Section 5 for details). Unlike MoS₂, the saturate I_d in WS₂ and WSe₂ devices is insensitive to thickness, whereas MoS₂ shows a logarithmic-like thickness dependence (Figure 3c). It is also interesting to note that the normalized saturation current in WSe₂ flakes is noticeably smaller than that in MoS₂ or WS₂ flakes with similar thickness.

Figure 4 encloses the backgate tunability data in WS₂ and WSe₂. In the presence of negative V_{bg} , the carrier concentration decreases with decreasing gate voltage in both WS₂ and WSe₂ following the expectation of capacitive model, which is opposite to the trend in MoS₂. Besides, the change in the carrier concentration is on the order of $1 \times 10^{13} \text{ cm}^{-2}$ in WS₂ and WSe₂, an order smaller than that in MoS₂. On the other hand, similar behavior has been observed in all the three materials in the presence of positive V_{bg} , apart from change in carrier concentration in MoS₂ and WS₂ are comparable and about 2 times larger than that in WSe₂.

The difference behavior in WS₂ and WSe₂ in comparison with MoS₂ can be explained qualitatively by the back tunneling process. First, WSe₂ has a much larger interlayer resistance than MoS₂^[54-56]. This is perhaps also the case for WS₂, since higher carrier concentration dramatically reduces interlayer resistivity^[56, 57]. When comparing MoS₂ with intrinsic doping induced by sulfur vacancy to WS₂ and WSe₂ which remain depleting intrinsically, it is natural that MoS₂ holds the smallest interlayer resistivity than WS₂ and WSe₂. Furthermore, characterization of interlayer resistivity through top-electrode/TMDs/bottom-electrode devices provides additional validation of the discussion above (see *Support Information* Section 8 for details). The back tunneling process in WS₂ and WSe₂ primarily occurs through the bulk channel in the vicinity of the interface whereas other bulk channels are well isolated from the interface, hence the saturation current is almost thickness independent. Second, the bulk channels in WS₂ and WSe₂ are almost empty in the absence of backgate voltage whereas they are partially occupied in MoS₂. Hence, a negative V_{bg} , which tries to deplete the channels, has little impact on the already almost empty bulk channels in WS₂ and WSe₂ in terms of the back tunneling process, instead, the trivial capacitive effect becomes explicit.

The bulk channels are far from fully occupied with the largest backgate voltage in our experiment, hence positive V_{bg} leads to similar results in all the three materials.

Through the comparison of these three TMDs, it highlights that enhance backgate tunability may be activated in material with suitable interlayer resistance and intrinsically partially occupied bulk channels. A more quantitative analysis would be beneficial to further optimise the backgate tunability, however, it is likely to require additional inputs such as the binding energy between the ions and the charge carrier in addition to the aforementioned interlayer resistance and intrinsic bulk channels occupancy, which calls for further investigation.

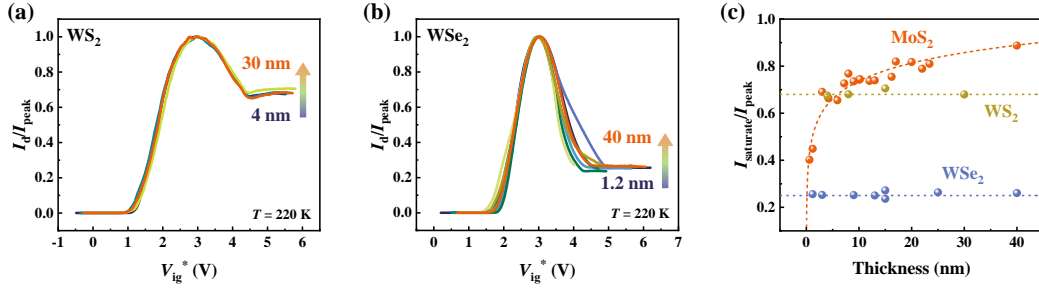


Figure 3. Thickness dependence of back tunneling process in WS₂ and WSe₂. a) & b) Rescaled transfer characteristic curves of WS₂ and WSe₂ device with various thicknesses, respectively. c) Comparison of the normalized saturation current in the three materials. Normalized saturation current is insensitive to flake thickness in WS₂ and WSe₂, whereas it shows a logarithmic-like reduction as a function of thickness in MoS₂.

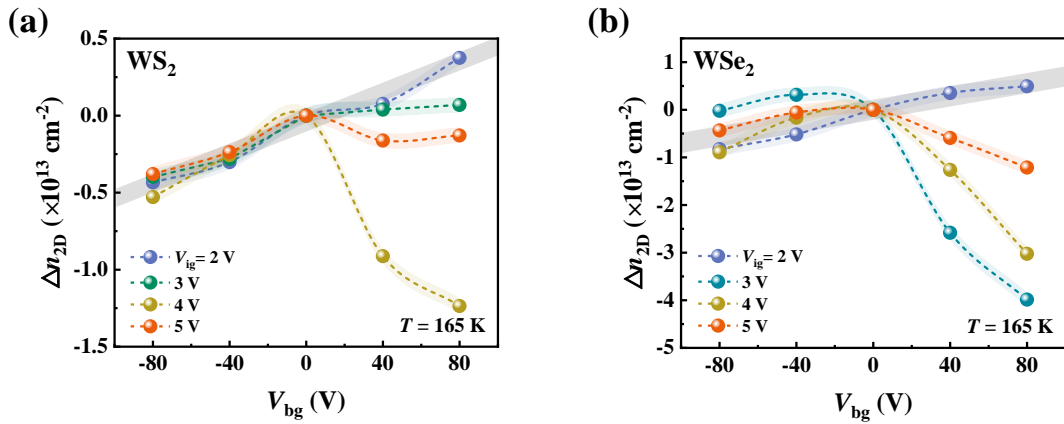


Figure 4. Backgate tunability in WS₂ and WSe₂ with a flake thickness of 10 nm. a) & b) Δn_{2D} as a function of backgate voltage with incremented V_{ig} in WS₂ and WSe₂, respectively, grey strip indicates the tunability based on the conventional capacitive model of bakcgate.

3. Conclusion

This work demonstrates the enhanced backgate tunability on interfacial carrier concentration in an ionic liquid-gated MoS₂ device by a conventional backgate. The main role of the backgate gate is tuning the bulk channels that mediates the back tunneling between the trapped bands forming at large ionic liquid gate voltage and interfacial channels, instead of inducing charge carrier via the trivial capacitive effect. The enhanced tunability of the backgate is key in utilizing the naturally existed periodic spatial modulation in an ionic liquid gated device to full potential, by addressing the issues of lacking of independent control on carrier concentration and periodic modulation potential.

4. Experimental Section

Crystal Exfoliation and Characterization: MoS₂ films were obtained from bulk MoS₂ (HQ Graphene Inc.) by mechanical exfoliation using Scotch tape and transferred onto 285 nm SiO₂/p-doped Si substrates^[58]. The thickness of the MoS₂ films was calibrated by atomic force microscope (AFM) (Bruker Dimension Edge Inc.), Raman spectroscopy, and optical microscope^[59].

Device Fabrication: MoS₂ flakes were selected and fabricated using a two-step EBL process, which utilized a bilayer resist consisting of Copolymer EL6 and PMMA 495A8. Following the first electron beam lithography (EBL, Crestec Inc.) step, standard Hall bar shapes were etched using reactive ion etching (RIE, Oxford Inc.)^[60]. After the second EBL step, Ti/Au (5/60 nm) was deposited and subsequent lift-off using acetone.

Electrical Measurement: All electrical measurements were conducted in a cryostat (TeslatronPT, Oxford Inc.). Transfer curve measurement utilized the Keithley 2634B source-measure unit, while the Hall effect and other transport experiments employed the Keithley 6221 current source and 2182A nanovoltmeter. It is necessary to stress that we have etched the flakes in to the shape of standard Hall bar to accurately quantify the carrier concentration. All transfer curve

measurements were systematically conducted at 220 K, slightly above the glass transition temperature (~ 190 K) of ionic liquid DEME-TFSI, to suppress interfacial electrochemical reactions^[21, 23], since the electrochemical window of ionic liquid exhibits significant temperature dependence, expanding from 3 V at 300 K to over 6.5 V at 220 K for DEME-TFSI^[51]. Concurrently, all the n_{2D} were acquired by Hall effect measurements at 165 K under continuous V_{ig} application throughout the cooling protocol (from 220 K to 165 K). This cryogenic protocol ensures frozen ion configurations, thereby eliminating dual-gate coupling effects^[53, 61] and enabling accurate determination of n_{2D} - V_{bg} relationships.

Acknowledgement

We acknowledge the financial support from the National Natural Science Foundation of China (Grant No. 12204184, 12074134).

Keywords

Ionic liquid, MoS₂, dual-gate, carrier concentration

References

- [1] Cherqui, C.; Bourgeois, M. R.; Wang, D.; Schatz, G. C. *Acc. Chem. Res.* **2019**, *52*, 2548.
- [2] Wang, D.; Guan, J.; Hu, J.; Bourgeois, M. R.; Odom, T. W. *Acc. Chem. Res.* **2019**, *52*, 2997.
- [3] Yu, S.; Wu, X.; Wang, Y.; Guo, X.; Tong, L. *Adv. Mater.* **2017**, *29*, 1606128.
- [4] Zhou, X.; Hung, Y.-C.; Wang, B.; Bansil, A. *Phys. Rev. Lett.* **2024**, *133*, 236401.
- [5] Cao, Y.; Fatemi, V.; Demir, A.; Fang, S.; Tomarken, S. L.; Luo, J. Y.; Sanchez-Yamagishi, J. D.; Watanabe, K.; Taniguchi, T.; Kaxiras, E.; et al. *Nature* **2018**, *556*, 80.
- [6] Guo, C.; Yu, J.; Deng, S. *Adv. Funct. Mater.* **2023**, *33*, 2302265.
- [7] Li, Y.; Li, Z.; Chi, C.; Shan, H.; Zheng, L.; Fang, Z. *Adv. Sci.* **2017**, *4*, 1600430.
- [8] Nayak, P. K.; Horbatenko, Y.; Ahn, S.; Kim, G.; Lee, J.-U.; Ma, K. Y.; Jang, A. R.; Lim, H.; Kim, D.; Ryu, S.; et al. *ACS Nano* **2017**, *11*, 4041.
- [9] Cao, Y.; Fatemi, V.; Fang, S.; Watanabe, K.; Taniguchi, T.; Kaxiras, E.; Jarillo-Herrero, P. *Nature* **2018**, *556*, 43.
- [10] Reddy, A. P.; Alsallom, F.; Zhang, Y.; Devakul, T.; Fu, L. *Phys. Rev. B* **2023**, *108*, 085117.
- [11] Cao, Y.; Rodan-Legrain, D.; Rubies-Bigorda, O.; Park, J. M.; Watanabe, K.; Taniguchi, T.; Jarillo-Herrero, P. *Nature* **2020**, *583*, 215.
- [12] Park, J. M.; Cao, Y.; Watanabe, K.; Taniguchi, T.; Jarillo-Herrero, P. *Nature* **2021**, *590*, 249.
- [13] Forsythe, C.; Zhou, X.; Watanabe, K.; Taniguchi, T.; Pasupathy, A.; Moon, P.; Koshino, M.; Kim, P.; Dean, C. R. *Nat. Nanotechnol.* **2018**, *13*, 566.
- [14] Barcons Ruiz, D.; Herzig Sheinfux, H.; Hoffmann, R.; Torre, I.; Agarwal, H.; Kumar, R. K.; Vistoli, L.;

- Taniguchi, T.; Watanabe, K.; Bachtold, A.; et al. *Nat. Commun.* **2022**, *13*, 6926.
- [15] Kim, D. S.; Dominguez, R. C.; Mayorga-Luna, R.; Ye, D.; Embley, J.; Tan, T.; Ni, Y.; Liu, Z.; Ford, M.; Gao, F. Y.; et al. *Nat. Mater.* **2023**, *23*, 65.
- [16] Zhang, Z.; Xie, J.; Zhao, W.; Qi, R.; Sanborn, C.; Wang, S.; Kahn, S.; Watanabe, K.; Taniguchi, T.; Zettl, A.; et al. *Nat. Mater.* **2024**, *23*, 189.
- [17] Gu, J.; Zhu, J.; Knuppel, P.; Watanabe, K.; Taniguchi, T.; Shan, J.; Mak, K. F. *Nat. Mater.* **2024**, *23*, 219.
- [18] Ye, J. T.; Zhang, Y. J.; Akashi, R.; Bahramy, M. S.; Arita, R.; Iwasa, Y. *Science* **2012**, *338*, 1193.
- [19] Li, L. J.; O'Farrell, E. C. T.; Loh, K. P.; Eda, G.; Özyilmaz, B.; Castro Neto, A. H. *Nature* **2015**, *529*, 185.
- [20] Leng, X.; Garcia-Barriocanal, J.; Bose, S.; Lee, Y.; Goldman, A. M. *Phys. Rev. Lett.* **2011**, *107*, 027001.
- [21] Bisri, S. Z.; Shimizu, S.; Nakano, M.; Iwasa, Y. *Adv. Mater.* **2017**, *29*, 1607054.
- [22] Saito, Y.; Nojima, T.; Iwasa, Y. *Supercond. Sci. Technol.* **2016**, *29*, 093001.
- [23] Ueno, K.; Shimotani, H.; Yuan, H.; Ye, J.; Kawasaki, M.; Iwasa, Y. *J. Phys. Soc. Jpn.* **2014**, *83*, 032001.
- [24] Xi, X.; Berger, H.; Forró, L.; Shan, J.; Mak, K. F. *Phys. Rev. Lett.* **2016**, *117*, 106801.
- [25] Ye, J. T.; Inoue, S.; Kobayashi, K.; Kasahara, Y.; Yuan, H. T.; Shimotani, H.; Iwasa, Y. *Nat. Mater.* **2009**, *9*, 125.
- [26] Ueno, K.; Nakamura, S.; Shimotani, H.; Ohtomo, A.; Kimura, N.; Nojima, T.; Aoki, H.; Iwasa, Y.; Kawasaki, M. *Nat. Mater.* **2008**, *7*, 855.
- [27] Jo, S.; Costanzo, D.; Berger, H.; Morpurgo, A. F. *Nano Lett.* **2015**, *15*, 1197.
- [28] Zeng, J.; Liu, E.; Fu, Y.; Chen, Z.; Pan, C.; Wang, C.; Wang, M.; Wang, Y.; Xu, K.; Cai, S.; et al. *Nano Lett.* **2018**, *18*, 1410.
- [29] Costanzo, D.; Jo, S.; Berger, H.; Morpurgo, A. F. *Nat. Nanotechnol.* **2016**, *11*, 339.
- [30] Chen, Q. H.; Lu, J. M.; Liang, L.; Zheliuk, O.; Ali, A.; Sheng, P.; Ye, J. T. *Phys. Rev. Lett.* **2017**, *119*, 147002.
- [31] Qin, M.; Han, X.; Ding, D.; Niu, R.; Qu, Z.; Wang, Z.; Liao, Z.-M.; Gan, Z.; Huang, Y.; Han, C.; et al. *Nano Lett.* **2021**, *21*, 6800.
- [32] Vo ĭchovsky, K.; Kuna, J. J.; Contera, S. A.; Tosatti, E.; Stellacci, F. *Nat. Nanotechnol.* **2010**, *5*, 401.
- [33] Manne, S.; Gaub, H. E. *Science* **1995**, *270*, 1480.
- [34] Page, A. J.; Elbourne, A.; Stefanovic, R.; Addicoat, M. A.; Warr, G. G.; Vo ĭchovsky, K.; Atkin, R. *Nanoscale* **2014**, *6*, 8100.
- [35] Elbourne, A.; Vo ĭchovsky, K.; Warr, G. G.; Atkin, R. *Chem. Sci.* **2015**, *6*, 527.
- [36] Yokota, Y.; Hara, H.; Harada, T.; Imanishi, A.; Uemura, T.; Takeya, J.; Fukui, K.-i. *Chem. Commun.* **2013**, *49*, 10596.
- [37] Bazant, M. Z.; Storey, B. D.; Kornyshev, A. A. *Phys. Rev. Lett.* **2011**, *106*, 046102.
- [38] Ivaništšev, V.; Fedorov, M. V. *Electrochem. Soc. Interface* **2014**, *23*, 65.
- [39] Ivaništšev, V.; O'Connor, S.; Fedorov, M. V. *Electrochem. Commun.* **2014**, *48*, 61.
- [40] Kirchner, K.; Kirchner, T.; Ivaništšev, V.; Fedorov, M. V. *Electrochim. Acta* **2013**, *110*, 762.
- [41] Zhou, S.; Panse, K. S.; Motevaselian, M. H.; Aluru, N. R.; Zhang, Y. *ACS Nano* **2020**, *14*, 17515.
- [42] Zhao, W.; Bi, S.; Balke, N.; Rack, P. D.; Ward, T. Z.; Kalinin, S. V.; Dai, S.; Feng, G. *ACS Appl. Mater. Interfaces* **2018**, *10*, 43211.
- [43] Lu, J.; Zheliuk, O.; Chen, Q.; Leermakers, I.; Hussey, N. E.; Zeitler, U.; Ye, J. *Proc. Nat. Acad. Sci.* **2018**, *115*, 3551.
- [44] Tjhe, D. H. L.; Ren, X.; Jacobs, I. E.; D'Avino, G.; Mustafa, T. B. E.; Marsh, T. G.; Zhang, L.; Fu, Y.; Mansour, A. E.; Opitz, A.; et al. *Nat. Mater.* **2024**, *23*, 1712.
- [45] Xie, W.; Liu, F.; Shi, S.; Ruden, P. P.; Frisbie, C. D. *Adv. Mater.* **2014**, *26*, 2527.
- [46] Panzer, M. J.; Frisbie, C. D. *JACS* **2007**, *129*, 6599.
- [47] Chen, Q.; Lu, J.; Liang, L.; Zheliuk, O.; Ali El Yumin, A.; Ye, J. *Adv. Mater.* **2018**, *30*, 1800399.

- [48] Piatti, E.; De Fazio, D.; Daghero, D.; Tamalampudi, S. R.; Yoon, D.; Ferrari, A. C.; Gonnelli, R. S. *Nano Lett.* **2018**, *18*, 4821.
- [49] Liao, M.; Zhu, Y.; Zhang, J.; Zhong, R.; Schneeloch, J.; Gu, G.; Jiang, K.; Zhang, D.; Ma, X.; Xue, Q.-K. *Nano Lett.* **2018**, *18*, 5660.
- [50] Lei, B.; Wang, N. Z.; Shang, C.; Meng, F. B.; Ma, L. K.; Luo, X. G.; Wu, T.; Sun, Z.; Wang, Y.; Jiang, Z.; et al. *Phys. Rev. B* **2017**, *95*, 020503.
- [51] Saito, Y.; Nakamura, Y.; Bahramy, M. S.; Kohama, Y.; Ye, J.; Kasahara, Y.; Nakagawa, Y.; Onga, M.; Tokunaga, M.; Nojima, T.; et al. *Nat. Phys.* **2015**, *12*, 144.
- [52] Ding, D.; Qu, Z.; Han, X.; Han, C.; Zhuang, Q.; Yu, X.-L.; Niu, R.; Wang, Z.; Li, Z.; Gan, Z.; et al. *Nano Lett.* **2022**, *22*, 7919.
- [53] Fuhrer, M. S.; Hone, J. *Nat. Nanotechnol.* **2013**, *8*, 146.
- [54] Na, J.; Shin, M.; Joo, M.-K.; Huh, J.; Jeong Kim, Y.; Jong Choi, H.; Hyung Shim, J.; Kim, G.-T. *Appl. Phys. Lett.* **2014**, *104*, 233502.
- [55] Das, S.; Appenzeller, J. *Nano Lett.* **2013**, *13*, 3396.
- [56] Shin, Y. S.; Lee, K.; Duong, D. L.; Kim, J. S.; Kang, W. T.; Kim, J. E.; Won, U. Y.; Lee, I.; Lee, H.; Heo, J.; et al. *Adv. Funct. Mater.* **2020**, *30*, 2003688.
- [57] Han, Y.; Chae, M.; Choi, D.; Song, I.; Ko, C.; Cresti, A.; Theodorou, C.; Joo, M.-K. *ACS Appl. Mater. Interfaces* **2023**, *15*, 58605.
- [58] Chang, R.; Chen, Q.; Shen, W.; Zhang, Y.; Zhang, B.; Wang, S. *Adv. Funct. Mater.* **2023**, *33*, 2301010.
- [59] Nie, C.; Zhang, B.; Gao, Y.; Yin, M.; Yi, X.; Zhao, C.; Zhang, Y.; Luo, L.; Wang, S. *J. Phys. Chem. C* **2020**, *124*, 16943.
- [60] Yi, X.; Song, Q.; Chen, Q.; Zhao, C.; Watanabe, K.; Taniguchi, T.; Chen, Q.; Yan, C.; Wang, S. *Nanotechnology* **2022**, *33*, 355601.
- [61] Domaretskiy, D.; Philippi, M.; Gibertini, M.; Ubrig, N.; Gutiérrez-Lezama, I.; Morpurgo, A. F. *Nat. Nanotechnol.* **2022**, *17*, 1078.